A Comparison Between Axisymmetric and Slab-Symmetric Cumulus Cloud Models

SU-TZAI SOONG AND YOSHIMITSU OGURA

Laboratory for Atmospheric Research, University of Illinois, Urbana 61801

(Manuscript received 11 December 1972)

ABSTRACT

Axisymmetric and slab-symmetric cumulus cloud models with Kessler's parameterizations for microphysical processes are developed. By using a staggered grid arrangement and applying a modified upstream difference scheme, erroneous behavior in the center of a simulated cloud, which would result with the use of the ordinary upstream difference scheme, is eliminated. A comparison between the present two models of different geometries confirms in general the conclusions reached in previous studies: the updraft in an aixsymmetric model grows more vigorously than in a slab-symmetric model. However, the ratio of the maximum updraft in the slab-symmetric model to that in the axisymmetric model is 0.53 in this study, notably larger than Murray's 0.12. An analysis of the pressure gradient force associated with cloud motions reveals that the vertical pressure gradient force due to perturbed pressure is: 1) of the same order of magnitude as that of the thermal buoyancy force in the core region of the cloud; is 2) acting in the opposite direction of the net force due to excess heat, moisture, and the weight of liquid water; and 3) is larger in absolute magnitude in the slab-symmetric model than in the axisymmetric one.

Also included are differences in the evolution of the modeled clouds in relation to different intensities of initial buoyant elements used in initiating convection in a conditionally unstable atmosphere and in relation to differences in the size of integration domains.

1. Introduction

Almost all cumulus clouds observed in the atmosphere show three-dimensional characteristics. However, presently available computers are not yet fast or large enough to allow investigation of the dynamics of a three-dimensional cloud by simulating it with much detail. The inclusion of environmental wind conditions and complicated microphysical processes leads to very large data fields if sufficient spatial resolution is used. For this reason, all modeling studies of moist convection published to date have been restricted to two-dimensions in space.

In two-dimensional cloud modeling, the geometry of the domain can be either slab-symmetric or axisymmetric. There is no doubt that the axisymmetric model is superior to the slab-symmetric model in single cloud simulation. In the axisymmetric model one is, however, unable to incorporate wind shear, an important factor in cloud dynamics. For this reason, Orville (1965, 1968), Liu and Orville (1969), Orville and Sloan (1970a), Lipps (1971), Takeda (1971) and Schlesinger (1972) have used slab-symmetric models.

A basic difference between clouds modeled in these two geometries was first discussed by Ogura (1963). Ogura noted that the ratio of maximum speed of compensating downdraft outside the cloud to the maximum speed of updraft inside the cloud in a slab-symmetric model is significantly larger than that in an axisymmetric model. A consequence of this strong downdraft in a slab-symmetric model is the generation of a region of relatively high excess temperature and low humidity outside the main body of the cloud, a physical situation unfavorable for sustained development of the primary cloud. For example, with a downdraft of 2 m $\sec^{-1}$ and a temperature lapse rate of 6C km^{-1}, the warming due to subsidence can result in a potential temperature increase of 5K in 10 min. This excess temperature is almost comparable in magnitude with the maximum excess temperature observed inside cumulonimbus.

A more systematic comparison between slab-symmetric and axisymmetric cloud models was made by Murray (1970). He also observed that the ratio of maximum downdraft speed to maximum updraft speed is larger in a slab-symmetric model than in an axisymmetric model, though the values of the ratio are a little different from those obtained by Ogura. The most striking point in Murray's result is that the cloud in an axisymmetric model grows vigorously with a maximum updraft of 17 m $\sec^{-1}$ at 32 min while the maximum updraft in a slab-symmetric model barely reached 2 m $\sec^{-1}$ at 29 min, the time computation was discontinued.

A recent comparison between clouds simulated in a two-dimensional slab-symmetric model and a three-dimensional model by Wilhelmson (1972) shows that the maximum vertical velocities are 11 and 16 m $\sec^{-1}$, respectively. The three-dimensional model simulated a single cloud at the center of the domain in a calm environment and the results should be close to those simulated in an axisymmetric model providing the initial and boundary conditions in the two models are the same. The initial and boundary conditions used by Murray in his axisymmetric model and by Wilhelmson in his three-dimensional model are by no means the same. It is purely by chance that their simulated maximum updraft velocities are similar. On the other hand, without changing the initial and boundary conditions, Wilhelmson's results show a marked difference from Murray's with regard to the maximum updraft in the slab-symmetric models.

The discrepancy between Murray's and Wilhelmson's results are the motivation of a more detailed study of the difference between an axisymmetric model and a slab-symmetric model. Also included here are differences in the evolution of modeled clouds in relation to different intensities of the initial buoyant element used in initiating convection in a conditionally unstable atmosphere and the relation of differences in the size of integration domains.

2. The basic equations

The basic equations used in this study are similar to those derived by Ogura and Phillips (1962) for deep moist convection. The modification by Wilhelmson and Ogura (1972) to include buoyancy of water vapor and the adoption of a non-isentropic base state has also been incorporated. The set of equations in cylindrical coordinates will be presented; those in Cartesian coordinates are similar but have fewer terms.

The horizontal and vertical equations of motion are

$$\frac{\partial u}{\partial t}=-u\frac{\partial u}{\partial r}-w\frac{\partial u}{\partial z}-C_p\bar{\theta}\frac{\partial \pi'}{\partial r}+F_r, \tag{1}$$

$$\frac{\partial w}{\partial t}=-u\frac{\partial w}{\partial r}-w\frac{\partial w}{\partial z}-C_p\bar{\theta}\frac{\partial \pi'}{\partial z}+g\left(\frac{\theta'}{\bar{\theta}}+0.61Q'_v-Q_c-Q_r\right)+F_z, \tag{2}$$

where u and w are the horizontal and vertical wind velocities, respectively, C_p the specific heat of dry air at constant pressure, θ the potential temperature, π the nondimensional pressure, g the acceleration of gravity, and Q_v the mixing ratio of water vapor. The ice phase of water is excluded and two classes of liquid water are considered: cloud droplets and raindrops. The mixing ratios are denoted by Q_c and Q_r, respectively. The terms F_r and F_z represent the horizontal and vertical components of the frictional force terms defined later. The barred variables represent those of the environmental base state. Deviations from these values are represented by primed variables. Any quantity not barred or primed represents the sum of the base state and the deviation. The equation of mass continuity for deep convection is

$$\frac{\partial r\bar{\rho}u}{\partial r}+\frac{\partial r\bar{\rho}w}{\partial z}=0, \tag{3}$$

where ρ is the density of the air. The nondimensional pressure π is related with the dimensional pressure p by

$$\pi=\left(\frac{p}{P}\right)^{R/C_p}, \tag{4}$$

where $P=1000$ mb (a reference pressure) and R is the gas constant of dry air. For simplicity in numerical integration, a vorticity equation is introduced. The vorticity is defined as

$$\eta=\frac{\partial\bar{\rho}u}{\partial z}-\frac{\partial\bar{\rho}w}{\partial r}. \tag{5}$$

Cross differentiating Eqs. (1) and (2) yields

$$\frac{\partial\eta}{\partial t}=-u\frac{\partial\eta}{\partial r}-w\frac{\partial\eta}{\partial z}+\left(\frac{2w}{\bar{\rho}}\frac{\partial\bar{\rho}}{\partial z}+\frac{u}{r}\right)\left(\eta-u\frac{\partial\bar{\rho}}{\partial z}\right)+uw\frac{\partial^2\bar{\rho}}{\partial z^2}-\bar{\rho}g\frac{\partial}{\partial r}\left(\frac{\theta'}{\bar{\theta}}+0.61Q'_v-Q_c-Q_r\right)+D_\eta, \tag{6}$$

where

$$D_\eta=\frac{\partial\bar{\rho}F_r}{\partial z}-\frac{\partial\bar{\rho}F_z}{\partial r}. \tag{7}$$

The term $-C_p(\partial\bar{\theta}\bar{\rho}/\partial z)(\partial\pi'/\partial r)$, which is typically two orders of magnitude smaller than the thermal buoyancy term, has been neglected in Eq. (6). The actual form of D_η used in computation will be presented later. A streamfunction ψ is defined in relation with u and w as

$$\frac{\partial\psi}{\partial z}=r\bar{\rho}u,\quad \frac{\partial\psi}{\partial r}=-r\bar{\rho}w. \tag{8}$$

Substituting (8) into (5) yields

$$\eta=\frac{1}{r}\frac{\partial^2\psi}{\partial z^2}+\frac{\partial}{\partial r}\left(\frac{1}{r}\frac{\partial\psi}{\partial r}\right). \tag{9}$$

With the boundary conditions of ψ in Section 3, Eq. (9) can be solved for ψ using the fast Fourier transformation scheme (Ogura, 1969). The wind components u and w can then be determined from (8). The equations for potential temperature, water vapor, cloud and rainwater content are, respectively:

$$\frac{\partial\theta'}{\partial t}=-u\frac{\partial\theta}{\partial r}-w\frac{\partial\theta}{\partial z}+\frac{L}{C_p\bar{\pi}}(P_2-P_3-P_4)+D_{\theta'} \tag{10}$$

$$\frac{\partial Q'_v}{\partial t}=-u\frac{\partial Q_r}{\partial r}-w\frac{\partial Q_v}{\partial z}-P_2+P_3+P_4+D_{Q'_v} \tag{11}$$

$$\frac{\partial Q_c}{\partial t}=-u\frac{\partial Q_c}{\partial r}-w\frac{\partial Q_c}{\partial z}-k_1(Q_c-a)$$
$$-k_2Q_cQ_r^{0.875}+P_2-P_3+D_{Q_c} \tag{12}$$

$$\frac{\partial Q_r}{\partial t}=-u\frac{\partial Q_r}{\partial r}-w\frac{\partial Q_r}{\partial z}+\frac{1}{\bar{\rho}}\frac{\partial}{\partial z}(\bar{\rho}V_rQ_r)$$
$$+k_1(Q_c-a)+k_2Q_cQ_r^{0.875}-P_4. \tag{13}$$

The diffusion terms will be discussed at the end of this section. In Eqs. (12) and (13), the assumption has been made that the cloud droplets have negligible terminal velocity and therefore always follow the air flow. The raindrop falls at a representative terminal velocity (denoted by V_r) relative to the air flow. The third term on the right-hand side of Eq. (13) accounts for the redistribution of rainwater as it falls. The representative terminal velocity is usually computed with the assumption of Marshall-Palmer distribution of Q_r and an equation to express the terminal velocity of individual raindrops as a function of its diameter (Kessler, 1969; Liu and Orville, 1969; Ogura and Takahashi, 1971). However, without assuming the Marshall-Palmer distribution, the representative terminal velocity can be derived directly from the empirical formula relating the rainwater content and the rainfall intensity (RI) derived by Marshall and Palmer (1948):

$$Q_r=72\times10^{-7}(RI)^{0.88}/\bar{\rho}, \tag{14}$$

where Q_r is in units of gm gm^{-1} and RI in mm hr^{-1}. The relation between RI and Q_r is

$$RI=360\bar{\rho}V_rQ_r. \tag{15}$$

Substituting (15) into (14) yields

$$V_r=3634(\bar{\rho}Q_r)^{0.1364}.$$

This equation gives a terminal velocity very close to that of the equation derived as volume-weighted mean by Ogura and Takahashi (1971). The value of V_r of Ogura and Takahashi is a little larger than that of this equation for small Q_r and is smaller for large Q_r.

In Eqs. (12) and (13), the rates of auto-conversion and collection are represented by Kessler's (1969) formulas with the parameters[1] $k_1=0$ for $Q_c\leqslant a$, $k_1=10^{-3}$ sec^{-1} for $Q_c>a$, $a=10^{-3}$ gm gm^{-1} and $k_2=2.2$. The term P_2 represents the rate of condensation which takes place whenever air is supersaturated. The amount of moisture condensed, which form cloud droplets only, is determined by the saturation technique (see Appendix).

Terms P_3 and P_4 represent the rate of evaporation of cloud droplets and raindrops, respectively. Cloud droplets are assumed to evaporate instantaneously if the air is not saturated. The rate of evaporation is determined so as to keep the air at the saturation level until the cloud droplets are totally evaporated. The raindrops will evaporate only if the cloud droplets are exhausted. The evaporation rate of raindrops is determined from the following equation which was used by Ogura and Takahashi (1971):

$$P_4=-\frac{1}{\bar{\rho}}\frac{[(Q_v/Q_{vs})-1]C(\bar{\rho}Q_r)^{0.525}}{5.4\times10^5+(0.41\times10^7/e_s)}, \tag{16}$$

where Q_{vs} is the saturation mixing ratio of water vapor, e_s the saturation vapor pressure (mb) over a plane water surface, and C the ventilation coefficient given by

$$C=1.6+0.57\times10^{-3}(V_r)^{1.5}. \tag{17}$$

The turbulent diffusion equation for isotropic turbulent mixing is used for $D_{\theta'}$, $D_{Q'_v}$ and D_{Q_c}. In the axisymmetric model, the diffusion for θ' is

$$D_{\theta'}=\frac{1}{r}\frac{\partial}{\partial r}Kr\frac{\partial\theta'}{\partial r}+\frac{1}{\bar{\rho}}\frac{\partial}{\partial z}K\bar{\rho}\frac{\partial\theta'}{\partial z}. \tag{18}$$

Similar equations apply to Q'_v and Q_c. The deviations of θ and Q_v from the base states are diffused in the hope of preserving the vertical profiles in the region far away from the cloud. The eddy diffusion coefficient K was proposed by Smagorinsky (1963) as a function of the deformation field. It was subsequently used by Deardorff (1970, 1972), and Wilhelmson and Ogura (1972). In the axisymmetric case, it is

$$K=(c\Delta)^2\left\{\left(\frac{\partial w}{\partial r}+\frac{\partial u}{\partial z}\right)^2\right.$$
$$\left.+2\left[\left(\frac{\partial u}{\partial r}\right)^2+\left(\frac{\partial w}{\partial z}\right)^2+\left(\frac{u}{r}\right)^2\right]\right\}^{\frac{1}{2}}, \tag{19}$$

where $\Delta=(\Delta r\Delta z)^{\frac{1}{2}}$ is a representative grid interval, Δr and Δz the horizontal and vertical grid intervals, respectively, and c a nondimensional constant chosen to be 0.2 following Deardorff[2] (1972). The same eddy diffusion coefficient is used for variables θ', Q'_v, and Q_c. There is no simple and definite expression to represent

---

[1] Kessler (1969) recommended the values of parameters $k_1=10^{-3}$ sec^{-1}, $a=5\times10^{-4}$ gm gm^{-1} and $k_2=2.2$. In a later version of his cumulus model, Kessler and Bumgarner (1971) used $k_1=10^{-4}$ sec^{-1} and $a=10^{-3}$ gm gm^{-1}. The results of some preliminary experiments using $a=10^{-3}$ gm gm^{-1}, $k_2=2.2$ and several different values for k_1 in the range from 10^{-4} to 10^{-3} sec^{-1} indicate that, as far as the fields of w, θ and Q_r are concerned, the differences are negligibly small, whereas Q_c at the cloud top shows some differences. For example, $Q_c=3.4$ gm gm^{-1} with $k_1=10^{-4}$ sec^{-1} and $Q_c=2.3$ gm gm^{-1} with $k_1=10^{-3}$ sec^{-1} at 15 min. Because 3.4 gm gm^{-1} of Q_c appears to be unrealistically large, $k_1=10^{-3}$ sec^{-1} is selected in this study.

[2] Deardorff used K in Eq. (19) for the eddy viscosity of momentum but increased K by a factor of 3 for the eddy diffusion coefficient of temperature in order to avoid excessive intensity at the larger wavenumbers in the temperature spectrum. Since this problem does not happen in the models of this study, K instead of $3K$ is used for the eddy diffusion coefficient in Eq. (18).

the effect of eddy viscosity on the variable η. The eddy viscosity for the momentum equations can be assumed as

$$\left.\begin{aligned} F_r&=\frac{1}{r}\frac{\partial}{\partial r}Kr\frac{\partial u}{\partial r}+\frac{1}{\bar{\rho}}\frac{\partial}{\partial z}K\bar{\rho}\frac{\partial u}{\partial z}-K\frac{u}{r^2}\\ F_z&=\frac{1}{r}\frac{\partial}{\partial r}Kr\frac{\partial w}{\partial r}+\frac{1}{\bar{\rho}}\frac{\partial}{\partial z}K\bar{\rho}\frac{\partial w}{\partial z}\end{aligned}\right\}. \tag{20}$$

Direct substitution of (20) into (7) leads to a complicated form of D_η, which is difficult to use. For this reason, the following assumption for D_η is made:

$$D_\eta=\frac{1}{r}\frac{\partial}{\partial r}Kr\frac{\partial \eta}{\partial r}+\frac{1}{\bar{\rho}}\frac{\partial}{\partial z}K\bar{\rho}\frac{\partial \eta}{\partial z}-K\frac{\eta}{r^2}. \tag{21}$$

The K for η is assumed the same as that for the other variables. The central difference is used in the finite-difference form of the diffusion terms so that the variables to be diffused are conserved.

3. Specifications of the experiment

a. The base state

The environmental condition, in which a cumulus cloud is to be simulated, is taken as the base state. For the purpose of studying the dynamics of the cumulus cloud, idealized temperature and humidity profiles closely related to those in the real tropical atmosphere are adopted. The temperature is assumed 25C at the surface, decreasing upward at the dry adiabatic lapse rate to the cloud base, which is assumed to be at 0.8 km from the surface. The relative humidity is 70% at the surface, increasing linearly to 90% at the cloud base. Above the cloud base, the relative humidity decreases at a rate of 7.5% km^{-1}. At higher levels, a minimum of 30% relative humidity is imposed to resemble the real atmosphere. The temperature lapse rate above the cloud base, denoted by Γ, is 6.0C km^{-1} in most of the cases. This temperature profile is conditionally unstable below about 5 km. A different lapse rate will be pointed out when it is used.

b. Boundary conditions

The top, bottom and lateral boundaries are assumed rigid with free slip conditions[3]:

$$\left.\begin{aligned} w&=0, \quad \frac{\partial\bar{\rho}u}{\partial z}=0, \quad \text{at } z=0,\, Z_H\\ u&=0, \quad \frac{\partial w}{\partial r}=0, \quad \text{at } r=D\end{aligned}\right\},$$

where Z_H is the height of the domain and D the distance between the center of the cloud to the lateral boundary. It is apparent from the above assumptions that $\eta=0$ and $\psi=0$ at all boundaries.

As will be described later, θ, Q_v, Q_c and Q_r are not defined on the boundaries, but rather in the grid box half a grid interval inside the boundaries. Since there is no interference between points inside and outside the boundaries, no physical boundary assumption is required. In computing eddy diffusion terms, the horizontal derivatives of these variables at lateral boundary and vertical derivatives at upper and lower boundaries are put to zero to avoid fictitious diffusion across the boundaries.

The main characteristic of the boundary conditions is that the domain is completely closed. The summation of Q_v, Q_c and Q_r integrated over the whole domain plus the amount of precipitation is always conserved. The integrated θ can only be changed by condensation and evaporation processes. Heat and moisture interaction between the air and the surface cannot take place in these boundary conditions. However, the effect of this kind of transfer is probably not important since the cloud lifetime is less than an hour.

c. The initial conditions

The base state with an initially buoyant element placed near the surface at the center of the domain composes the initial condition. This buoyant element has a region of excess potential temperature computed according to

$$\theta'=\theta_0\left\{1-\left[\frac{z_0-z}{z_0-(\Delta z/2)}\right]^2\right\}\left(1-\frac{x^2}{x_0{}^2}\right),$$

where θ_0 is the maximum initial excess potential temperature at the central axis at level z_0. In this study, $x_0=1.2$ km and $z_0=1.0$ km are adopted. The level of maximum θ' is then located at the center of the grid box immediately above the cloud base. The maximum θ' does not equal θ_0 because of the grid arrangement. The value of θ_0 is taken to be 0.5K. Smaller values are also used to investigate the effect of θ_0 on the cloud development (Section 8).

The relative humidity above the cloud base inside the region of positive θ', and one grid box beyond it at the top and the sides, is assumed 100%. The saturation process, hence, will begin after the first time step of integration. This initial condition is adequate to study the dynamics of the cumulus cloud. When investigating the initiation of cumuli, some other initial conditions should be used.

---

[3] The free slip condition at lower boundary does not take into account the surface frictional force and is not realistic. An alternate lower boundary condition, which parameterizes the frictional effect at the surface in such a way that the horizontal velocity at the surface is half the magnitude of the velocity a grid above the surface, has been tested. Since the simulated clouds under the two different lower boundary conditions have only a negligible difference, the free slip boundary condition is used for simplicity.

4. The finite-differencing scheme

The limited core storage of currently available computers poses a major problem in cloud simulation. The forward time difference is usually adopted in order to reduce the core storage requirement despite the fact that the truncation error in time is first order. With a forward time difference, the simplest and most stable space difference is the upstream scheme. Crowley (1968) and Molenkamp (1968) have noted that the upstream scheme has a large implicit diffusion. Crowley also developed stable second-order and fourth-order space difference schemes, which have a smaller implicit diffusion. However, Orville and Sloan (1970b) compared Crowley's second-order scheme against the upstream scheme and found the results concerning the formation and evolution of the cloud in a slab-symmetric model quite similar. Thus, the upstream scheme, with its simplicity and stability, is more attractive. Furthermore, Crowley's second-order scheme produces spurious oscillations in a two-dimensional advection experiments (Crowley, 1968; Schlesinger, 1972). This oscillation can increase the water content substantially because all negative values generated have to be replaced by zero. Crowley also developed second-order and fourth-order conservative schemes, but they possess the same problem found in the non-conservative scheme mentioned above.

In the preliminary stage of this study, the upstream scheme in advective form was used and unrealistic results were produced at the central axis of the cloud. In order to make this point clear, the prognostic equation of a variable F in an axisymmetric cloud simulation model with the source and diffusion terms neglected is considered. It can be written either in advective form

$$\frac{\partial F}{\partial t}=-u\frac{\partial F}{\partial r}-w\frac{\partial F}{\partial z},\tag{22}$$

or in flux form

$$\frac{\partial F}{\partial t}=-\frac{1}{r\bar{\rho}}\frac{\partial}{\partial r}(r\bar{\rho}uF)-\frac{1}{r\bar{\rho}}\frac{\partial}{\partial z}(r\bar{\rho}wF).\tag{23}$$

Eq. (23) can be derived from Eq. (22) by using Eq. (3), the mass continuity equation. Eqs. (22) and (23) represent the same physical phenomenon and should give an identical result. However, their finite-difference representation is different and Eq. (23) in finite-difference form conserves the variable F integrated over a closed domain.

In cloud modeling, conservation of heat, moisture and water substances are quite important. When Eq. (22) is used, it does not conserve these variables and may pose a serious problem on the model, especially at the central axis. In finite-difference form, the value at a grid point represents the mean value over the elemental volume encompassing the point. This mean value at the central axis is modified by horizontal inflow as well as vertical inflow. However, the horizontal wind velocity is zero at the central axis and the value of F will not be affected by horizontal advection if Eq. (22) is used. Hence, the results at the central axis, which in turn affects the whole simulated cloud, can be quite unrealistic. The fact that the central axis attracts the most attention from the cloud modeler accentuates the problem. For this reason the following "modified upstream" scheme is used for the variables θ, Q_v, Q_c and Q_r.

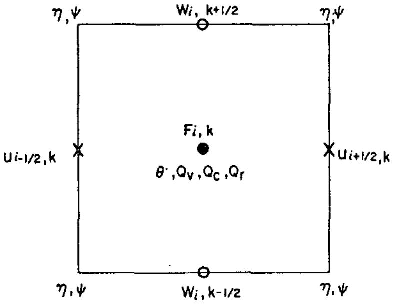

FIG. 1. The staggered grid arrangement used in the modified upstream difference scheme.

With a staggered grid arrangement as shown in Fig. 1, the finite-difference form of Eq. (23) can be written as

$$\left(\frac{\partial F}{\partial t}\right)_{i,k}=-\left[(r_{i+\frac12}\bar{\rho}u_{i+\frac12}F_{i+\frac12}-r_{i-\frac12}\bar{\rho}u_{i-\frac12}F_{i-\frac12})_k/\Delta r\right.$$
$$\left.+(r\bar{\rho}_{k+\frac12}w_{k+\frac12}F_{k+\frac12}-r\bar{\rho}_{k-\frac12}w_{k-\frac12}F_{k-\frac12})_i/\Delta z\right]/r_i\bar{\rho}_k.\tag{24}$$

The four terms in parentheses represent the inflow or outflow of F through the four boundaries. Assuming F is uniform in the volume, then

$$F_{i+\frac12,k}=\begin{cases}F_{i,k}, & \text{if } u_{i+\frac12}>0\\ F_{i+1,k}, & \text{if } u_{i+\frac12}<0\end{cases}\tag{25}$$

The same conditions apply to $F_{i-\frac12,k}$, $F_{i,k+\frac12}$ and $F_{i,k-\frac12}$. To illustrate the scheme in an example, assume

$$\left.\begin{matrix}u_{i+\frac12,k}<0, & u_{i-\frac12,k}>0\\ w_{i,k+\frac12}>0, & w_{i,k-\frac12}>0\end{matrix}\right\}.$$

Then

$$\left(\frac{\partial F}{\partial t}\right)_{i,k}=-\left[(r_{i+\frac12}\bar{\rho}u_{i+\frac12}F_{i+1}-r_{i-\frac12}\bar{\rho}u_{i-\frac12}F_{i-1})_k/\Delta r\right.$$
$$\left.+(r\bar{\rho}_{k+\frac12}w_{k+\frac12}F_k-r\bar{\rho}_{k-\frac12}w_{k-\frac12}F_{k-1})_i/\Delta z\right]/r_i\bar{\rho}_k.\tag{26}$$

Eq. (3) can be written as

$$(r_{i+\frac12}\bar{\rho}u_{i+\frac12}-r_{i-\frac12}\bar{\rho}u_{i-\frac12})_k/\Delta r$$
$$+(r\bar{\rho}_{k+\frac12}w_{k+\frac12}-r\bar{\rho}_{k-\frac12}w_{k-\frac12})_i/\Delta z=0.\tag{27}$$

Substituting the third term of Eq. (27) into Eq. (26),

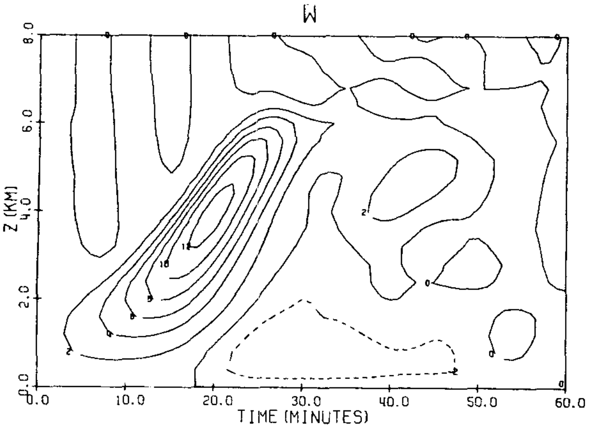

FIG. 2. Time-height variation of w at the central axis of the axisymmetric model: $\Gamma=6.0\text{C km}^{-1}$, $D=12.8$ km, $\theta_0=0.5$K. Contours range from -2 to 12 m sec^{-1} with a contour interval of 2 m sec^{-1}.

we have

$$\left(\frac{\partial F}{\partial t}\right)_{i,k}=-\{[r_{i+\frac{1}{2}}\bar{\rho}u_{i+\frac{1}{2}}(F_{i+1}-F_i)/\Delta r]_k$$
$$+[r_{i-\frac{1}{2}}\bar{\rho}u_{i-\frac{1}{2}}(F_i-F_{i-1})/\Delta r]_k$$
$$+[r\bar{\rho}_{k-\frac{1}{2}}w_{k-\frac{1}{2}}(F_k-F_{k-1})/\Delta z]_i\}/r_i\bar{\rho}_k. \quad (28)$$

This form is very similar to the upstream space difference. It sums up advection at inflow boundaries but disregards the outflow boundary. In computation, either (26) or (28) may be used. This scheme has a truncation error of the first order in space and has some characteristics of the regular upstream scheme, i.e., implicit diffusion and high stability, but the variable F is conserved and the central axis problem is eliminated. For a special case of two-dimensional non-divergent channel flow, this difference scheme reduces to the upstream scheme. Consequently, the name "modified upstream" scheme is adopted. It is natural to place η and ψ at the corners of the grid box because of the location of u and w. The regular upstream scheme is used for the advection of η because otherwise many averages on η (or u and w) are needed.

Throughout this study, the space increment $\Delta r=\Delta z=400$ m and time increment $t=20$ sec are used. The height of the integration domain is 12.8 km and the distance between the center of the cloud to the lateral boundary is also 12.8 km except for the cases in Section 9. In the following five sections, the result of experiments will be presented.

5. The dynamics of cloud in the axisymmetric model

The time-height variation of w, θ' and Q_r at the central axis of the axisymmetric model is shown in Figs. 2, 3 and 4, respectively. The characteristics of cloud development pertinent to these time-height variations can be visualized in four distinct regions.

I. The region above the cloud top.
II. The region characterizing the path of the initial buoyant element.
III. The region around cloud base, including the sub-cloud layer.
IV. The layer between regions II and III.

The four regions are shown schematically in Fig. 5. Region II is the region of active cloud growth, which rises with time. Regions III and IV are characterized by weaker disturbances left in the wake of the rising buoyant element.

The air in Region I oscillates regularly with a period of 10 min. This oscillation is initiated by the adiabatic cooling above the rising cloud. The same kind of oscillation can be generated in the model by imposing a small initial temperature excess, which is not capable of producing a cloud. A cloud top oscillation with the same period is also evident in the one-dimensional model of Ogura and Takahashi (1973).

In Region II, the maximum w reaches 12.9 m sec^{-1} at 20 min. The level of maximum w ascends gradually in the first 10 min, and changes to a rapid ascending rate of 4.5 m sec^{-1} during the next 20 min. It reaches a height of 7 km at 30 min, and levels off thereafter as w diminishes. The ascending rates for the level of maximum θ', and the cloud top, which is essentially the same as the upper limit of Q_r, are similar to that of the level of maximum w. The maximum θ' reaches 3.1K at 18 min, and the maximum Q_r is 5.2 gm kg^{-1} at 23 min. In the active cloud growing stage between 10 and 30 min, the rising rate of the cloud top is about half the speed of the average maximum updraft during that period, which incidentally coincides with the "rule of thumb" indicated by Murray (1970). Because every 3 gm kg^{-1} liquid water content has a drag force equivalent to a deficit of potential temperature about 1K, the weight of Q_r has

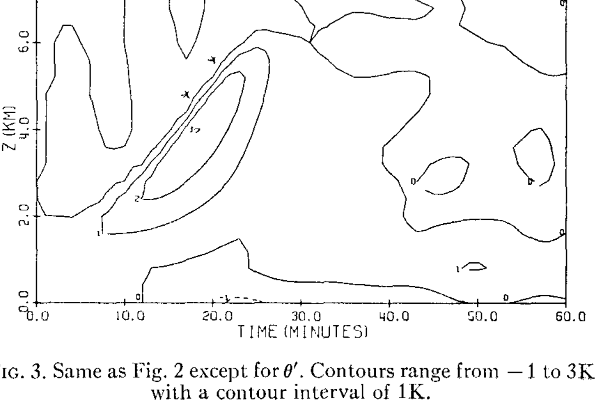

FIG. 3. Same as Fig. 2 except for θ'. Contours range from -1 to 3K with a contour interval of 1K.

to be the major factor causing the maximum w to decrease after 20 min. The continuous decrease of w after 30 min, when Q_r has been reduced, is due to entrainment, cloud top evaporation, and moist adiabatic ascending in a conditionally stable environment which causes a negative potential temperature.

In Region III, the rainwater falls to the cloud base at 12 min and the subsequent evaporation causes a rapid decrease of θ' in the sub-cloud layer. As a result, the updraft in the sub-cloud layer decreases and turns into a downdraft at 18 min. The weight of the raindrops contributes to the increase of downdraft speed after its initial development. The downdraft in this region persists for more than 30 min, with a maximum speed of 3.8 m sec^{-1} at 27 min. The Q_r is also a maximum at 27 min in this region.

The main feature of Region IV is the development of a second maximum updraft at a level 4.5 km above ground. The evolution of characteristics of this region should be traced back to Region II, where w at this level is a maximum at 20 min. This updraft decreases drastically when entering Region IV, developing into a downdraft at 30 min. This downdraft is initiated from below in Region III and extends to a maximum height of 4.8 km at 33 min. Since the negative θ' is confined in Region III, it is apparent that the upward extension of the downdraft into Region IV is due to the weight of liquid water content. Between 25 and 45 min, θ' in Region IV is approximately 0.5K and changes only slightly. The Q_r decreases from about 5 gm kg^{-1} to 0.5 gm kg^{-1} in the same period. As a result, the buoyancy force is then capable of producing a second maximum updraft of 3.5 m sec^{-1} at 41 min. After the decay of the second maximum w, gravity waves are dominant and no more physically significant phenomenon develops.

Ogura and Takahashi (1971, 1973) have developed a one-dimensional time-dependent model. In that model, a cloud is envisioned to take a cylindrical form with a time-independent radius, and the pressure perturbation associated with the cloud motion is ignored. Furthermore, the environmental atmosphere surrounding the cloud is assumed to be at rest all the time so that no variations with time take place. The environmental conditions and microphysical processes involved in the model are different from those applied in the present study. Nevertheless, a comparison between the time-height variation of the vertical velocity in the one-dimensional model and Fig. 2 of this paper shows some interesting qualitative differences.

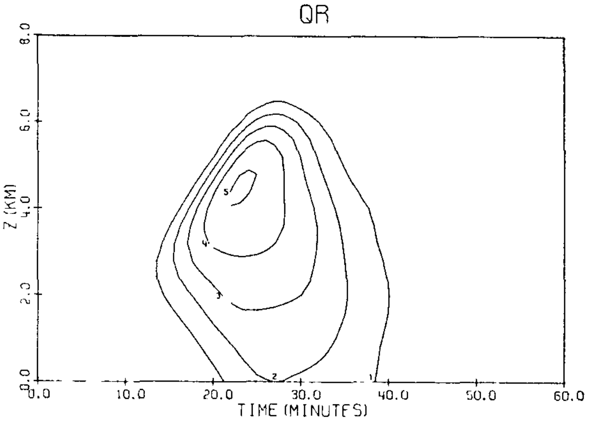

FIG. 4. Same as Fig. 2 except for Q_r. Contour range from 1 to 5 gm kg^{-1} with a contour interval of 1 gm kg^{-1}.

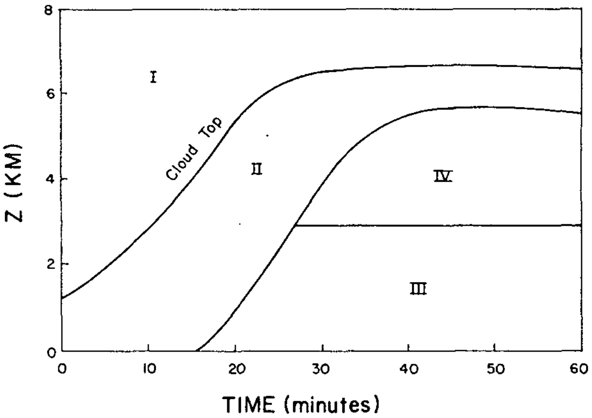

FIG. 5. Schematic illustration of the characteristics of cloud development.

First, the maximum vertical velocity in the one-dimensional model is located very close to the top of the cloud (see Fig. 3 of the 1971 paper and Fig. 2 of the 1973 paper). Consequently, the horizontal outflow from the cloud satisfying the mass continuity is extremely strong and concentrated in a thin layer near the cloud top (Fig. 3 of 1973 paper). This is not the case in Fig. 2 for the axisymmetric cloud. Holton (1973) has also shown that the unrealistically strong outflow in a one-dimensional model can be alleviated by incorporating the pressure perturbation.

Second, in Ogura and Takahashi's cloud, all meteorological variables in Regions III and IV reach a steady state and remain in that state until the downdraft develops inside the cloud. This is again quite different from the distributions shown in Figs. 2–4 in this paper. The unrealistic behavior in the one-dimensional model is obviously caused by ignoring variations which should take place in the environment: the relatively dry downdraft develops outside the cloud to compensate the updraft in the developing stage and this dry air is subsequently fed into the cloud.

6. Cloud dynamics in the slab-symmetric model

The time-height variation of w, θ' and Q_r at the central plane of the slab-symmetric model are shown in Figs. 6, 7 and 8, respectively. The basic characteristics of cloud development are similar to those of axisymmetric model, even though the cloud grows

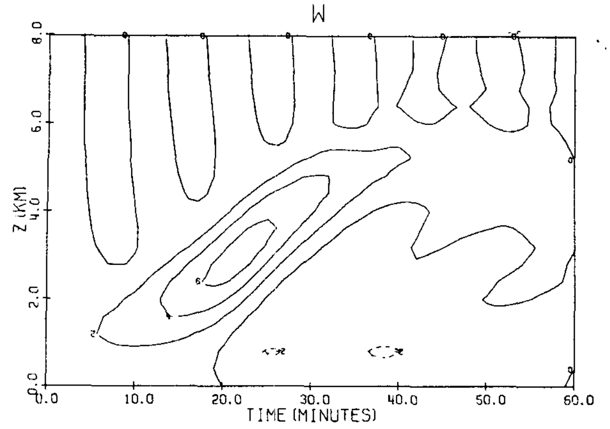

FIG. 6. Time-height variation of w at the central plane of the slab-symmetric model: $\Gamma=6.0$C km^{-1}, $D=12.8$ km, $\theta_0=0.5$K. Contour range from -2 to 6 m sec^{-1} with a contour interval of 2 m sec^{-1}.

smaller and slower in the slab-symmetric model. The maximum w reaches only 6.9 m sec^{-1} at 21 min, the maximum θ' is 2.6K at the same time, and the maximum Q_r is 2.3 gm kg^{-1} at 25 min. During the active growing stage of the cloud between 10 and 30 min, the ascending rate of the level of maximum w, that of maximum θ', and that of the cloud top are approximately 2.8 m sec^{-1}, which is also about half of the mean maximum updraft during that period. The updraft in the main body of the cloud (Region II) lasts much longer in the slab-symmetric model, and the secondary maximum updraft below the cloud top (Region IV) is not so obvious. In order to match the magnitudes of the maximum updraft of the slab-symmetric model to that of the axisymmetric model, the temperature lapse rate above the cloud base is increased from 6 to 6.6C km^{-1} in the slab-symmetric model. The resulting maximum values of w, θ' and Q_r along the central plane are plotted in Fig. 9 along with those values corresponding to lapse rate of 6C km^{-1} in both models. The increase of lapse rate in the slab-symmetric model results in a faster growth of the cloud after the first few minutes. The w and Q_r curves are surprisingly close to those of the axisymmetric model and suggests a similar cloud behavior. The maximum θ' increases to 5K and can be accounted on the basis of the steeper lapse rate. There is also a tendency to produce a secondary maximum updraft at 40 min, but the magnitude is not large. The three Q_r curves reach about the same value after 45 min, indicating that the lifetime of the three cases is not significantly different.

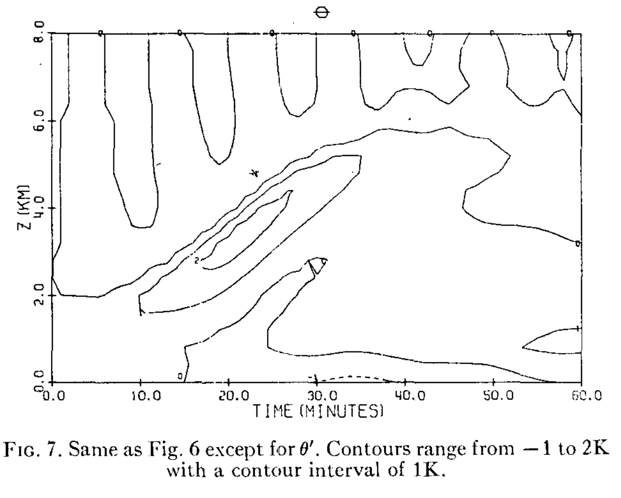

FIG. 7. Same as Fig. 6 except for θ'. Contours range from -1 to 2K with a contour interval of 1K.

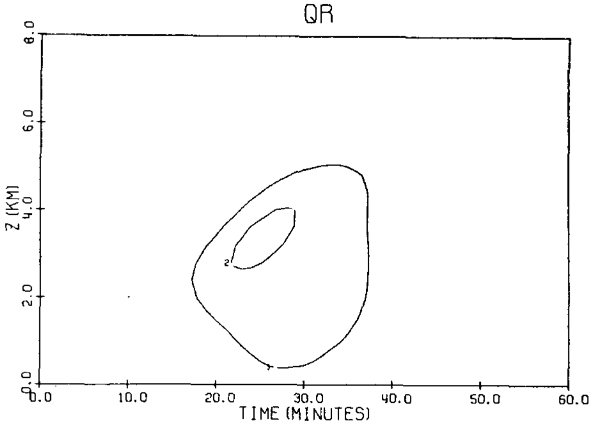

FIG. 8. Same as Fig. 6 except for Q_r. Contours range from 1 to 2 gm kg^{-1} with a contour interval of 1 gm kg^{-1}.

Fig. 10 shows a further comparison of the w field between the axisymmetric model with $\Gamma=6$C km^{-1} and the slab-symmetric model with $\Gamma=6.6$C km^{-1} at 20 min. As noted above, the maximum vertical velocities in these two cases are similar in magnitude. The sizes of the updraft region as shown in Fig. 10 are also similar. The difference is in the downdraft: the maximum downdraft in the axisymmetric model is 3.1 m sec^{-1} whereas that in the slab-symmetric model is 5.6 m sec^{-1}. Moreover, the downdraft region extends far away from the cloud region in the slab-symmetric model: even at the point 5.2 km from the center of the cloud, the maximum downdraft is approximately 0.5 m sec^{-1} whereas the downdraft in the axisymmetric model is confined in the region of 3.2 km radius from the central axis.

7. The role of pressure deviation in the development of a cloud

To clarify the cause of the difference between the growth rates of the axisymmetric and slab-symmetric clouds described above, the vertical momentum equation is again displayed:

$$\frac{dw}{dt}=-C_p\bar{\theta}\frac{\partial\pi'}{\partial z}+g\left(\frac{\theta'}{\bar{\theta}}+0.61Q'_v-Q_c-Q_r\right)+F_z.$$

Considering the central axis at time zero, the buoyancy force due to θ' and Q'_v in the two geometries are exactly the same. The frictional force and the drag due to liquid water content are identically zero. Consequently, the pressure gradient force is the only force that may generate different w in the two geometries for the first few time steps. In this article, we have introduced the streamfunction and the pressure field was not calculated in time iterations. However, the values of the pressure gradient term were estimated as a residue from the above equation. These values across the level of maximum w in Region II in the two geometries at 5-min intervals are listed in Table 1. At time zero, this level is chosen to be the level of maximum w at the first time step. The values of θ', Q'_v and Q_c+Q_r at these levels are listed for comparison. After 35 min in the axisymmetric model and 45 min in the slab-symmetric model, the location of the maximum w in Region II cannot be determined and the results are not presented. The pressure gradient force is apparently always acting in the opposite direction of the net force due to excess heat, moisture and the weight of liquid water. Its magnitude in equivalence of potential temperature deviation is -0.42K in the axisymmetric model and -0.55K in the slab-symmetric one at time zero. They are large enough to compensate the thermal buoyancy force, which is 0.42K. Adding up the thermal buoyancy force, the water vapor buoyancy force (which is equivalent to 0.34K) and the pressure gradient force, the net force is then 0.34K for the axisymmetric model and 0.21K for the slab-symmetric model. The smaller net force in the slab-symmetric model prevents the cloud from rising at the same rate as in the axisymmetric model. The slower increase in the maximum w in the slab-symmetric model is apparent in Fig. 9. The difference between the downward pressure gradient forces in the slab-symmetric model and in the axisymmetric model increases from 0.13K at time zero to 0.43K at 20 min. This difference, which is caused by the difference in geometry, will eventually result in a larger w and higher cloud in the axisymmetric model than in the slab-symmetric model. The ratio of the absolute magnitude of the pressure gradient force to the thermal buoyancy force at the mature stage is about one-third for the axisymmetric model and larger than one-half for the slab-symmetric model. It should be emphasized that even with a pressure gradient force $\leqslant -0.75$K, as in the axisymmetric model, its effect should not be neglected. Schlesinger (1972) has also pointed out in his slab-symmetric modeling study of deep moist convection

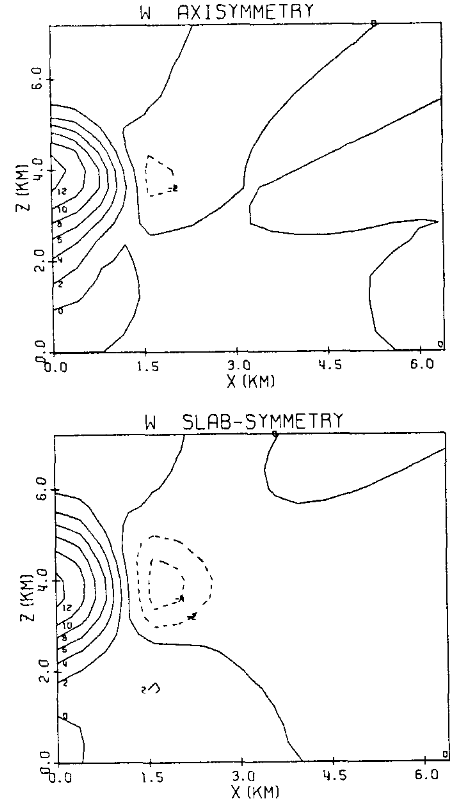

FIG. 10. Distribution of w on x, z plane near the center of cloud at 20 min. $\Gamma=6.0$C km^{-1} for the axisymmetric model and $\Gamma=6.6$C km^{-1} for the slab-symmetric model. $D=12.8$ km, $\theta_0=0.5$K. Contours range from -4 to 12 m sec^{-1} with a contour interval of 2 m sec^{-1}.

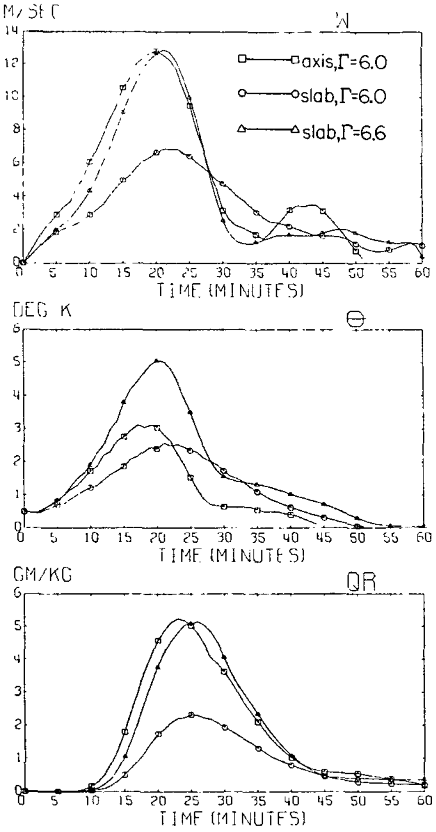

FIG. 9. Time variation of maximum w, θ' and Q_r at the central axis of the axisymmetric model with $\Gamma=6.0$C km^{-1} and those at the central plane of the slab-symmetric model with $\Gamma=6.0$C km^{-1} and $\Gamma=6.6$C km^{-1}: $D=12.8$ km, $\theta_0=0.5$K.

TABLE 1. The thermal and water vapor buoyancy, liquid water drag, and vertical pressure gradient forces at the level of maximum vertical velocity at the central axis (all units in equivalant °K).

Time (min)	Height (km)	w (m sec^{-1})	θ'	Q'_v	$Q_c + Q_r$	P*	S**
Axisymmetric model							
0	1.2	0.0	0.42	0.34	0.0	−0.42	0.76
5	1.3	2.96	0.59	0.38	−0.15	−0.48	0.82
10	1.9	6.09	1.49	0.50	−0.59	−0.68	1.40
15	2.8	10.56	2.37	0.58	−1.14	−0.75	1.81
20	4.0	12.87	2.63	0.52	−1.74	−0.68	1.41
25	5.2	9.47	1.46	0.36	−1.72	−0.23	0.10
30	5.8	3.26	0.21	0.27	−0.83	0.17	−0.35
35	5.9	1.76	−0.27	0.25	−0.26	0.26	−0.28
Slab-symmetric model							
0	1.2	0.0	0.42	0.34	0.0	−0.55	0.76
5	1.3	1.83	0.50	0.36	−0.09	−0.61	0.77
10	1.6	2.91	0.97	0.43	−0.34	−0.83	1.06
15	2.1	5.02	1.61	0.52	−0.66	−0.95	1.47
20	2.7	6.70	1.96	0.54	−0.90	−1.11	1.60
25	3.6	6.40	1.90	0.49	−0.96	−1.26	1.43
30	4.4	4.74	1.54	0.42	−0.78	−1.15	1.81
35	4.9	3.05	1.01	0.36	−0.55	−0.83	0.82
40	5.3	2.22	0.59	0.32	−0.37	−0.52	0.54
45	5.3	1.65	0.29	0.30	−0.27	−0.24	0.32

* $P=-C_p\bar{\theta}(\partial\pi'/\partial z)$.
** $S=\theta'+Q'_v+Q_c+Q_r$.

that the pressure gradient force is roughly half as large as the thermal buoyancy force in the strongest part of the updraft and this force is acting downward.

The deviation of pressure from its base state affects the cloud development in two ways. First, as described above, it is responsible for a pressure gradient force, which directly contributes to the change of horizontal and vertical momentum. Second, it affects the determination of temperature, which in turn is used along with the potential temperature to determine the saturation vapor pressure. In the second way, the pressure deviation acts indirectly on the cloud development through the condensation process. Wilhelmson and Ogura (1972) have investigated the second effect and they pointed out that $\pi'/\bar{\pi}$ is an order of magnitude less than $\theta'/\bar{\theta}$ in the cloud region, i.e.,

$$\frac{\pi'}{\bar{\pi}} \ll \frac{\theta'}{\theta}. \tag{29}$$

The pressure deviation can then essentially be ignored in determining the saturation vapor pressure. This was demonstrated by Wilhelmson and Ogura in several numerical experiments, with and without considering π' in the saturation technique.

Eq. (29) does not imply that the pressure gradient force is also an order of magnitude smaller than the thermal buoyancy force:

$$H\frac{\partial\pi'}{\partial z} \ll \frac{\theta'}{\theta}, \tag{30}$$

where $H[=C_p\bar{\theta}/g]$ is the scale height of an isentropic atmosphere with a typical potential temperature $\bar{\theta}$. On the contrary, as discussed above, the pressure gradient force and the thermal buoyancy force in the region of the cloud are of the same order of magnitude, i.e.,

$$H\frac{\partial\pi'}{\partial z} \approx \frac{\theta'}{\bar{\theta}}. \tag{31}$$

The main reason why (31) rather than (30) is valid in the cloud region is the concentration of the pressure gradient near the center of the cloud. The magnitude of H, which is about 30 km, is also a factor of 3 larger than the vertical dimension of the domain. Consequently, $H(\partial\pi'/\partial z)$ is one order of magnitude larger than π', and Eq. (29) leads to Eq. (31).

It should be noted that the computed π' and $\partial\pi'/\partial z$ are dependent on the definition of θ'. This can be illustrated using a simple example of a domain with a horizontally uniform slab of air where $\theta'>0$. This situation will result in no motion because the horizontal derivative of the potential temperature is zero and no vorticity can be generated. The vertical momentum equation reduces to

$$C_p\bar{\theta}\frac{\partial\pi'}{\partial z} = g\frac{\theta'}{\bar{\theta}}. \tag{32}$$

The system is still in a state of hydrostatic balance even though π and θ deviate from their base state values. If θ' is defined as the deviation of θ from a horizontal mean value instead of from a base state value, the above situation will give $\theta'=0$ for the warmer slab of air and hence $\pi'=0$ provided the pressure deviation is zero somewhere in the domain. The location of the zero pressure deviation is chosen to be at the upper left corner of the domain in the model of Wilhelmson and Ogura (1972). This π' is now defined as the deviation of π from the new hydrostatic equilibrium state derived from the new profile of θ with the warmer slab of air. A similar definition for Q'_v also requires a hydrostatic readjustment. The simulated cloud will not change for either definition of θ' and Q'_v, but the explanation of the force terms will be different. For θ' defined as the deviation from the horizontal mean, it will, in general, be smaller than when using the other definition because of the general warming due to subsidence outside the cloud and due to condensation in the cloud. At the same time, the π' and $\partial\pi'/\partial z$ terms will also become smaller. This difference is more obvious in the slab-symmetric model because it results in strong subsidence warming. As the domain of integration increases, the horizontal mean θ will approach θ of the base state. For this reason, the definition of θ' as the deviation of θ from its base state value is preferred.

8. Effect of the initial buoyant element on cloud simulation

As described in Sections 5 and 6 the development of a cloud simulated in this study is very similar to those of Murray's in the axisymmetric model, but differs greatly in the slab-symmetric one. The results of Wilhelmson's model are close to those of this study in both geometries. The ratio of the maximum w between slab-symmetric and axisymmetric models in this study is 0.53, which is a little smaller than Wilhelmson's 0.71, but far larger than Murray's 0.12. Murray used excess moisture for the initial buoyant element, while in this study and that of Wilhelmson's, both excess temperature and moisture are used. The very large difference between the axisymmetric model and the slab-symmetric model of Murray's was then thought to be caused by the initial buoyant element he used. For this reason, simulations were made in which θ_0 was reduced to 0.3K, 0.1K and 0K for both geometries.

For the case of $\theta_0=0$, the humidity field is rounded off on the edge of the initial buoyant element: the relative humidities are 100, 97, 95 and 90 percent, respectively, for grid boxes 1 to 4 from the central axis. Without rounding off the edge of the moisture field for the case of $\theta_0=0$, the edge of the initial buoyant element will rise at a faster rate than the center. This does not cause any serious trouble in the axisymmetric model, because w in the center gradually catches up and the center eventually becomes the dominant region of updraft in the whole domain after 15 min. However, in the slab-symmetric case, the maximum w in the central plane always lags behind the air surrounding it, and there are clouds formed at both sides of the central plane. The maximum w at the central plane never reaches 1 m sec^{-1}, and it turns into a downdraft as the two clouds beside it grow.

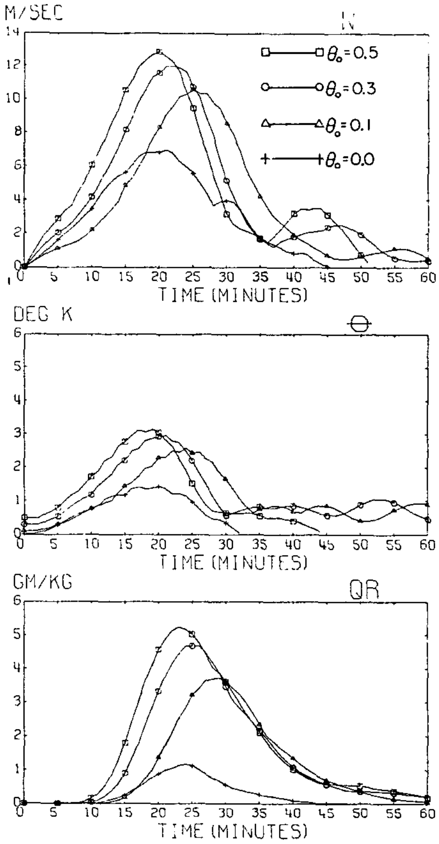

FIG. 11. Time variation of maximum w, θ' and Q_r at the central axis of the axisymmetric model for different θ_0: $\Gamma=6.0$C km^{-1}, $D=12.8$ km.

The results of the maximum w, θ' and Q_r at the central axis using a different θ_0 for the initial disturbance in the axisymmetric and slab-symmetric models are shown in Figs. 11 and 12, respectively. These maximum values tend to be smaller and reach their peak later in time with decreasing θ_0 for both geometries, except for the case of $\theta_0=0$. In addition, the second maximum w in the axisymmetric model is not so obvious as θ_0 becomes smaller. The maximum Q_r for $\theta_0=0.5$K, 0.3K and 0.1K is similar after 30 min in the axisymmetric case and 35 min in the slab-symmetric one, indicating that the lifetime of the simulated cloud is not altered greatly by changing θ_0. As for the case of $\theta_0=0$, the maximum w, θ' and Q_r are much smaller than the other cases, but they reach their maxima at about the same time as in the case of $\theta_0=0.5$K. The ratio of the maximum w between the slab-symmetric model and the axisymmetric model does decrease slightly with decreasing θ_0, but not to the extent that Murray's results indicate.

9. The effect of domain size on cloud simulation

The boundary conditions used in this model close the domain completely. There is no exchange of momentum, heat, moisture or liquid water across the boundaries.

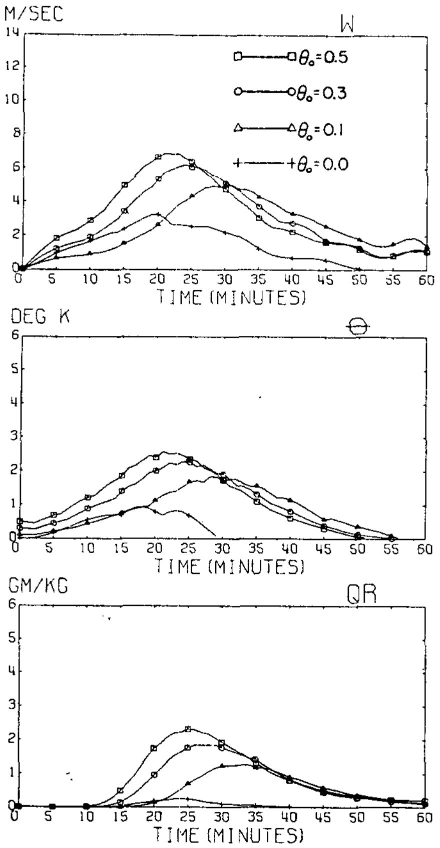

FIG. 12. Same as Fig. 1 except at the central plane of the slab-symmetric model.

These boundary conditions are by no means realistic because, in the real atmosphere, disturbances produced by clouds are not confined in a finite domain. There is no unique way to determine variable boundary conditions; hence their use may not bring the cloud model any closer to reality. As a matter of fact, Takeda (1971) found that the variations of air flow at the lateral boundaries due to cloud disturbances were not described by the use of his "open" boundary conditions in which the wind field is allowed to change at the boundaries. With closed boundary conditions, the boundary effects should be very small during cloud lifetimes of about an hour if a large enough domain is used.

To determine the required minimum domain, the model is tested for $D=6.4$, 12.8 and 25.6 km with other conditions being kept unchanged. The time variation of the maximum w, θ' and Q_r at the central axis for the axisymmetric and the slab-symmetric models are shown in Figs. 13 and 14, respectively. For the axisymmetric model, the w's for $D=12.8$ and 25.6 km show little difference before 35 min. During that time, the growth and decay of the first peak of w is completed. After 35 min, the w's in the two domain sizes reach the same second peak value with a phase difference of 2–3 min. The θ's and Q_r's in the two domain sizes begin to deviate after 25 min, but the differences are within 0.1K for θ' and 0.1 gm kg^{-1} for Q_r. The case of $D=6.4$ km gives a peak w almost 1 m sec^{-1} less than the cases of larger domain. The second w peak is very small and behaves quite differently from the other cases. A large difference in θ' from the larger domain cases is also observed after 25 min. The value of Q_r is smaller than the other cases, which can be accounted for by the weaker updraft as well as the limited moisture supply due to the limited domain.

The effects of domain size on the slab-symmetric model are tested with a steeper lapse rate of 6.6C km^{-1} above the cloud base to simulate a cloud similar to that of the axisymmetric model with a lapse rate of 6.0C km^{-1}. As in the axisymmetric model, the case of $D=6.4$ km shows a remarkable difference from cases with a larger domain. The differences between $D=12.8$ and 25.6 km are small during the growth stage but are consistently larger during the decay stage, especially for the variables θ' and Q_r. As far as the dynamics of cloud development are concerned, $D=12.8$ km is acceptable for both geometries, even though the slab-symmetric model seems to need a larger domain. The different response on domain size in the two geometries can be explained by the larger percentage of area occupied by

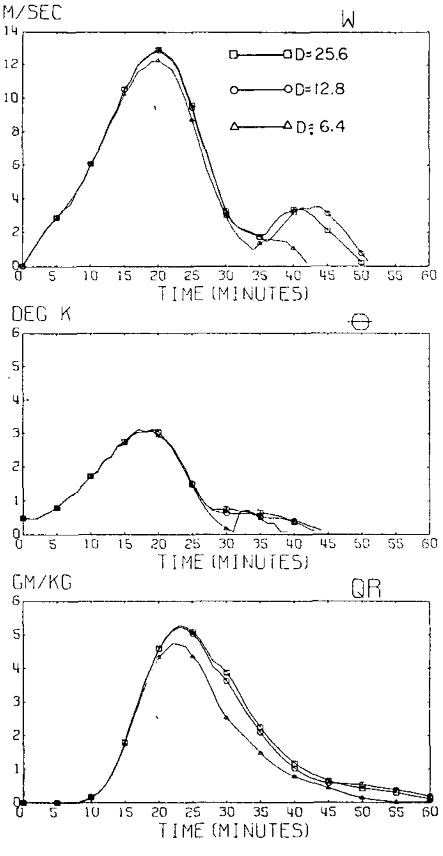

FIG. 13. Time variation of maximum w, θ' and Q_r at the central axis of the axisymmetric model for different domain sizes D (km): $\Gamma=6.0$C km^{-1}, $\theta_0=0.5$K.

the updraft in the slab-symmetric model. It also should be noted that the domain requirement is dependent on the size and height of the simulated cloud. If a larger and taller cloud is to be simulated, a larger domain may be needed.

10. Summary and concluding remarks

In this article, axisymmetric and slab-symmetric cumulus cloud models are developed. By using a staggered grid arrangement and applying a modified upstream difference scheme, erroneous behavior in the center of a simulated cloud, which would result with the use of the ordinary upstream difference scheme, is eliminated. A comparison between results using the present axisymmetric model and with those of Ogura and Takahashi's one-dimensional model (1971, 1973) reveals some shortcomings in dynamical formulation of the latter. The present axisymmetric model is currently being extended to investigate the development of warm rain, as an extension of the study by Ogura and Takahashi.

The effect of the size of an integration domain on cloud simulation is also investigated. It is demonstrated that unless the domain is sufficiently large, the downdraft outside the cloud will be intensified and moisture supply will be limited with the use of an artificial rigid lateral boundaries. This strong downdraft will significantly affect the evolution of the simulated cloud.

As for the comparison between axisymmetric and slab-symmetric models, the present result confirms in general the conclusions reached in previous studies by Ogura (1963), Murray (1970) and Wilhelmson (1972): the updraft in an axisymmetric model grows more vigorously than in a slab-symmetric model for the same environmental and initial conditions; the ratio of the maximum speed of the compensating downdraft outside the cloud to the maximum updraft speed in a slab-symmetric model is significantly larger than that in an axisymmetric model; and the compensating downdraft in a slab-symmetric model spreads in space more widely than in an axisymmetric model.

The analysis of the pressure gradient force associated with cloud motion is made to clarify the role of the pressure variation in the development of a cloud. It is found that the vertical pressure gradient force due to pressure variations is of the same order of magnitude as that of the thermal buoyancy force in the core region of the cloud. At all times this pressure gradient force is acting in the opposite direction of the net force due to excess heat, moisture, and the weight of liquid water. The pressure force in a slab-symmetric model is larger in absolute magnitude than that in an axisymmetric model. This is responsible for the slower increase in maximum w in the slab-symmetric model.

The only significant difference between the present results and those of Murray is in the ratio of the maximum w between slab-symmetric and axisymmetric models: It is 0.53 in this study and 0.12 in Murray's. The cause for this difference remains unclear. Because the evolution of a simulated cloud depends significantly on the environmental conditions, particularly on moisture content in the lower layers, it is probable that the base state chosen in Murray's experiment happens to be just above the marginal state for the development of a slab-symmetric cloud.

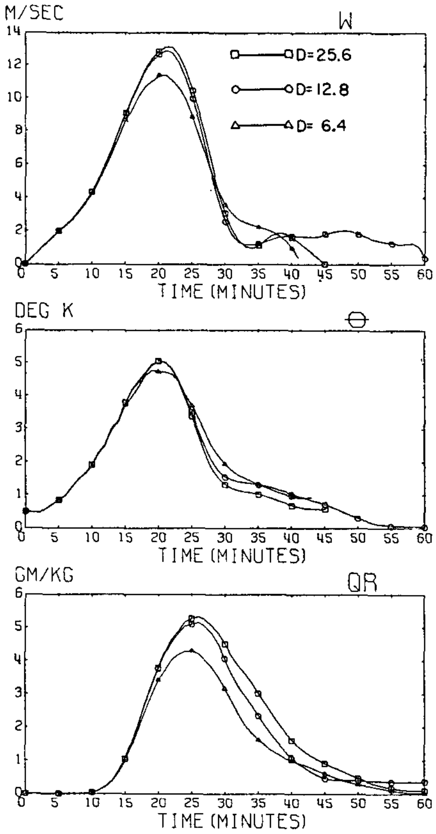

FIG. 14. Same as Fig. 13 except at the central plane of the slab-symmetric model with $\Gamma=6.6$C km^{-1}, $\theta_0=0.5$K.

Acknowledgments. The authors wish to thank Robert Wilhelmson for useful discussions and improving the original manuscript, and Claire Farris for typing the manuscript. The present work was supported by the Advanced Research Project Agency under Contract DAHCO4 71 C 0016.

APPENDIX

Saturation Technique

With θ and Q_v given at $t=\tau$, dummy values θ^* and Q_v^* at $t=\tau+1$ are first calculated at each grid point, taking into account only the dynamical terms (advection and diffusion) in the prognostic Eqs. (10) and (11). The saturation mixing ratio corresponding to θ^* is then calculated, using Teten's formula

$$Q^*_{vs}=b\exp[a(\pi_e\theta^*-273)/(\pi_e\theta^*-36)], \qquad \text{(A1)}$$

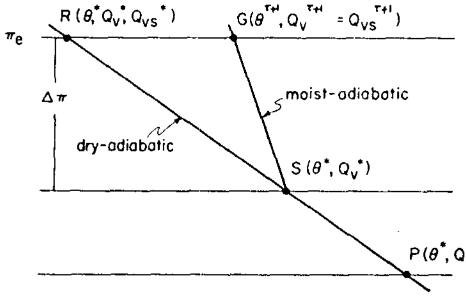

FIG. A1. Schematic diagram of the saturation technique.

where $b=3.8/p_e$, $a=7.5\ \ln 10$, and p_e and π_e are, respectively, the dimensional and non-dimensional pressure at that grid point. If $Q^*_v>Q^*_{vs}$ at a grid point (denoted by G in Fig. A1), the air is supersaturated. Because we do not permit the air to be supersaturated, $\theta^{\tau+1}$ and $Q_v^{\tau+1}$at G must be recalculated from θ^* and Q^*_v so that $\theta^{\tau+1}$and $Q_v^{\tau+1}$ satisfy the relation

$$Q_v^{\tau+1}=Q_{vs}^{\tau+1}=b\exp[a(\pi_e\theta^{\tau+1}-273)/(\pi_e\theta^{\tau+1}-36)]. \quad \text{(A2)}$$

This may be done in the following way: Consider an air parcel that is lifted from a point P up to a grid point G during a time step from τ to $\tau+1$. Because it is saturated at G, it must become saturated at a level (denoted by S) between P and G, inclusively. Along the path PS on the adiabatic chart in Fig. A1, θ and Q_v take the values θ^* and Q^*_v, respectively, as they are conserved. Along the path SG, the air is in the moist adiabatic process and the changes of potential temperature and saturation mixing ratio are related by

$$d\theta=-\frac{L}{C_p\bar{\pi}}dQ_{vs}. \quad \text{(A3)}$$

To the first order of accuracy in finite-difference form, Eq. (A3) is approximated by

$$\Delta\theta=\theta^{\tau+1}-\theta^*=\frac{L}{C_p\bar{\pi}}(Q^*_v-Q_{vs}^{\tau+1}), \quad \text{(A4)}$$

where

$$\bar{\pi}=\pi_e+(\Delta\pi/2), \quad \text{(A5)}$$

and $\Delta\pi$ is the non-dimensional pressure difference between S and G. Substituting $\theta^{\tau+1}$ in the first part of (A4) into (A2), and retaining only the terms of the first order of $\Delta\theta$, we get the following approximate expression for $Q_{vs}^{\tau+1}$:

$$Q_{vs}^{\tau+1}=Q^*_{vs}\left[1+\frac{237a\Delta\theta\pi_e}{(\pi_e\theta^*-36)^2}\right]. \quad \text{(A6)}$$

By substituting Eq. (A6) into the second part of Eq. (A4) and collecting the terms of $\Delta\theta$, we get

$$\Delta\theta\left[1+\frac{237a\pi_eQ^*_{vs}}{(\pi_e\theta^*-36)^2}\frac{L}{C_p\bar{\pi}}\right]=\frac{L}{C_p\bar{\pi}}(Q^*_v-Q^*_{vs}). \quad \text{(A7)}$$

If we define

$$r_1=\left[1+\frac{237a\pi_eQ^*_{vs}}{(\pi_e\theta^*-36)^2}\frac{L}{C_p\bar{\pi}}\right]^{-1}, \quad \text{(A8)}$$

Eq. (A7) then becomes

$$\theta^{\tau+1}=\theta^*+\frac{Lr_1}{C_p\bar{\pi}}(Q^*_v-Q^*_{vs}). \quad \text{(A9)}$$

It also follows that

$$Q_{vs}^{\tau+1}=Q^*_v-r_1(Q^*_v-Q^*_{vs}). \quad \text{(A10)}$$

Eqs. (A9) and (A10) give the new values of θ and Q_v at $t=\tau+1$, respectively.

The value of $\bar{\pi}$ in (A9) and (A10) can be determined as follows. First, the relation between the dimensional and non-dimensional pressures at the point S is given by

$$p_e+\Delta p=P(\pi_e+\Delta\pi)^{1/\kappa}\approx p_e\left(1+\frac{1}{\kappa}\frac{\Delta\pi}{\pi_e}\right). \quad \text{(A11)}$$

Teten's formula applied at the point S is

$$Q^*_v=\frac{3.8}{p_e+\Delta p}\exp\left\{\frac{a[(\pi_e+\Delta\pi)\theta^*-273]}{(\pi_e+\Delta\pi)\theta^*-36}\right\}. \quad \text{(A12)}$$

Taking the terms of the first order of $\Delta\pi$ in Eq. (A12), Eq. (A12) is approximated by

$$Q^*_v=Q^*_{vs}\left[1+\frac{237a\Delta\pi\theta^*}{(\pi_e\theta^*-36)^2}\right]\left(1+\frac{\Delta\pi}{\kappa\pi_e}\right)^{-1}. \quad \text{(A13)}$$

Consequently,

$$\Delta\pi=(Q^*_v-Q^*_{vs})\left[\frac{237a\theta^*Q^*_{vs}}{(\pi_e\theta^*-36)^2}-\frac{Q^*_v}{\kappa\pi_e}\right]^{-1}. \quad \text{(A14)}$$

Eqs. (A5) and (A14) give the required $\bar{\pi}$.

Eqs. (A8), (A9) and (A10) are very similar to a set of equations derived by Asai (1965). However, the physical processes implied in the two sets of equations are different. In Asai's approach, an air parcel is first lifted up dry adiabatically to the level of the grid point G (denoted as R in Fig. A1) and then θ and Q_v are readjusted isobarically at the pressure p_e so that air is brought to exact saturation. Our approach is more direct: it computes $\theta^{\tau+1}$ and $Q_{vs}^{\tau+1}$ by going through PSG rather than PRG in Asai's approach. The pressure variation in the condensation process between S and G has been taken into account as $\bar{\pi}$ appears in Eqs. (A9) and (A10). Another difference is that the Clasius-Clapeyron equation is used in Asai's equations to compute the variation of Q_{vs} with respect to θ, while Teten's formula is used in our model. However, it is mentioned that, with the vertical resolution of the model used in this study, the two methods are found to give no significant difference in the actual computation of evolution of clouds.

REFERENCES

Asai, T., 1965: A numerical study of the air-mass transformation over the Japan Sea in winter. *J. Meteor. Soc. Japan*, **43**, 1–15.

Crowley, W. P., 1968: Numerical advection experiments. *Mon. Wea. Rev.*, **96**, 1–11.

Deardorff, J. W., 1970: A numerical study of three-dimensional turbulent channel flow at large Reynolds numbers. *J. Fluid Mech.*, **41**, 453–480.

, 1972: Numerical investigation of neutral and unstable planetary boundary layers. *J. Atmos. Sci.*, **29**, 91–115.

Holton, J. R., 1973: A one dimensional model including pressure perturbation. *Mon. Wea. Rev.*, **101** (in press).

Kessler, E., 1969: On the distribution and continuity of water substance in atmospheric circulation. *Meteor. Monogr.*, **10**, No. 32, 84 pp.

——, and W. C. Bumgarner, 1971: Model of precipitation and vertical air currents. NOAA Tech. Memo. ERL NSSL-54, 93 pp.

Lipps, F. B., 1971: Two-dimensional numerical experiments in thermal convection with vertical shear. *J. Atmos. Sci.*, **28**, 3–19.

Liu, J. Y., and H. D. Orville, 1969: Numerical modeling of precipitation and cloud shadow effects on mountain-induced cumuli. *J. Atmos. Sci.*, **26**, 1283–1298.

Marshall, J. S., and W. McK. Palmer, 1948: The distribution of raindrops with size. *J. Meteor.*, **5**, 165–166.

Molenkamp, C. R., 1968: Accuracy of finite-difference methods applied to the advection equation. *J. Appl. Meteor.*, **7**, 160–167.

Murray, F. W., 1970: Numerical models of a tropical cumulus cloud with bilateral and axial symmetry. *Mon. Wea. Rev.*, **98**, 14 28.

Ogura, M., 1969: A direct solution of Poisson's equation by dimension reduction method. *J. Meteor. Soc. Japan*, **47**, 319–323.

Ogura, Y., 1963: The evolution of a moist convective element in a shallow, conditionally unstable atmosphere: A numerical calculation. *J. Atmos. Sci.*, **20**, 407–424.

——, and N. A. Phillips. 1962: A scale analysis of deep and shallow convection in the atmosphere. *J. Atmos. Sci.*, **19**, 173–179.

——, and T. Takahashi, 1971: Numerical simulation of the life cycle of a thunderstorm cell. *Mon. Wea. Rev.*, **99**, 895–911.

——, and ——, 1973: The development of warm rain in a cumulus model. *J. Atmos. Sci.*, **30**, 262–277.

Orville, H. D., 1965: A numerical study of the initiation of cumulus cloud over nountain terrain. *J. Atmos. Sci.*, **22**, 684–699.

——, 1968: Ambient wind effects on the initiation and development of cumulus clouds over mountains. *J. Atmos. Sci.*, **25**, 385–403.

——, and L. J. Sloan, 1970a: A numerical simulation of the life history of a rainstorm. *J. Atmos. Sci.*, **27**, 1148–1159.

——, and ——, 1970b: Effects of higher order advection techniques on a numerical cloud model. *Mon. Wea. Rev.*, **98**, 7–13.

Schlesinger, R. E., 1972: A numerical model of deep moist convection: The influence of ambient conditions and internal physical mechanisms. Annual Report—1971, Vol. 1, University of Wisconsin, 149–356.

Smagorinsky, J., 1963: General circulation experiments with the primitive equations: I. The basic experiment. *Mon. Wea. Rev.*, **91**, 99–164.

Takeda, T., 1971: Numerical simulation of a precipitating convective cloud: The formation of a "long-lasting" cloud. *J. Atmos. Sci.*, **28**, 350–376.

Wilhelmson, R., 1972: The numerical simulation of a thunderstorm cell in two- and three-dimensions. Ph.D. thesis, University of Illinois.

——, and Y. Ogura, 1972: The pressure perturbation and the numerical modeling of a cloud. *J. Atmos. Sci.*, **29**, 1295–1307.